Bringing the Ends together: Cryo-EM structures of mycobacterial Ku in complex with DNA define its role in NHEJ synapsis

Joydeep Baral[1,2,3,5], Ching-Seng Ang[4], Paul James McMillan[3,6], Kalyan Shobhana[3,6], Elizabeth Hinde[2*], Amit Kumar Das[1*], Isabelle Rouiller[3,5*]

[1] *Department of Bioscience and Biotechnology, Indian Institute of Technology Kharagpur, West Bengal, India*

[2] *School of Physics, University of Melbourne, Victoria, Australia*

[3] *Department of Biochemistry and Pharmacology, Bio21 Molecular Science and Biotechnology Institute, University of Melbourne, Victoria, Australia*

[4] *Melbourne Mass Spectrometry and Proteomics Facility, The Bio21 Molecular Science and Biotechnology Institute, The University of Melbourne, Parkville, Victoria, 3010, Australia*

[5] *Australian Research Council Centre for Cryo-Electron Microscopy of Membrane Proteins, Parkville, VIC 3052, Australia*

[6] *Biological Optical Microscopy Platform, University of Melbourne, Victoria, Australia*

* Corresponding authors

E-mail: isabelle.rouiller@unimelb.edu.au (I.Rouiller) - *For Correspondence*
amitk@bt.iitkgp.ac.in (A.K.Das)
elizabeth.hinde@unimelb.edu.au (E.Hinde)

Abstract:

Non-homologous end joining (NHEJ) is the sole pathway for repairing double-strand breaks (DSBs) in *Mycobacterium tuberculosis* during dormancy, relying on mycobacterial Ku (mKu) and ligase D, with mKu as the rate-limiting factor. Despite its essential role, the lack of structural information on prokaryotic Ku has hindered understanding of the molecular mechanisms underlying bacterial two-component NHEJ machinery. Here, we present the first cryo-EM structures of mKu in DNA-bound and higher-order super-complex forms, revealing a Ku-mediated DNA synapsis mechanism unique to prokaryotes. Integrating cryo-EM with hydrogen-deuterium exchange mass spectrometry (HDX-MS), we define key mKu-mKu dimerization, DNA-binding, and synapsis interactions essential for efficient NHEJ, bridging structure with function. In silico mutagenesis and predictive structural modeling identify residues critical for DNA binding and synapsis, with mutations destabilizing synapsis and impairing NHEJ repair. Förster resonance energy transfer (FRET) confirms DNA-dependent mKu oligomerization in solution, while live-cell imaging captures its spatiotemporal dynamics during DSB repair. These findings provide fundamental insights into the architecture and function of prokaryotic NHEJ, positioning mKu as a potential therapeutic target against tuberculosis and offering a framework for understanding DNA repair across bacterial species.

Keywords:

Non-homologous end joining (NHEJ); DNA synapsis; Double-strand breaks (DSBs); Ku; *Mycobaterium tuberculosis*

Introduction:

Mycobacterium tuberculosis (Mtb), the causative agent of tuberculosis, encounters constant threats to its genomic integrity from both environmental stressors and intrinsic factors(1). As an intracellular pathogen, Mtb resides within host macrophages in a dormant, non-replicating state(2). During dormancy, the pathogen is exposed to genotoxic agents such as reactive oxygen and nitrogen species, leading to substantial DNA damage, particularly double-stranded DNA breaks (DSBs)(3). DSBs are one of the most deleterious forms of genetic damage, as they threaten genome stability and cell viability. Consequently, efficient DNA repair is essential for Mtb's survival in the hostile host environment[3].

Among the available repair mechanisms, the non-homologous end joining (NHEJ) pathway is uniquely capable of repairing DSBs in non-replicating cells(4). Unlike homologous recombination, which requires a template, NHEJ operates in a template-independent manner, making it indispensable during dormancy. The ability to exploit this pathway as a therapeutic target is particularly compelling when paired with DSB-inducing agents, offering new avenues to combat drug-resistant tuberculosis(5).

Bacterial NHEJ is significantly simpler than its eukaryotic counterpart, relying on two core components: the Ku protein and ATP-dependent DNA ligase D (LigD)(6,7). Ku binds to DNA ends, stabilizing them and protecting them from exonucleolytic degradation(8). It subsequently recruits LigD via its C-terminal tail, anchoring it to the damaged site(9). Together, these proteins form a minimal repair apparatus capable of ligating broken DNA ends(6).

A key step in NHEJ is DNA synapsis—the alignment and stabilization of broken DNA ends to enable ligation(10). Without intervention, exposed DNA ends are highly flexible and diffuse freely in solution. While the eukaryotic NHEJ apparatus has been extensively studied, with detailed 3D structures of synaptic complexes available(11), the mechanisms underlying bacterial DNA synapsis remain poorly understood. Current knowledge is limited to the two-component bacterial system, leaving significant gaps in understanding how synapsis is achieved and whether additional factors are involved(12).

Our recent studies on mycobacterial Ku (mKu) have shown its ability to form higher-order oligomeric complexes in the presence of DNA(8). However, whether this oligomerization is sufficient to mediate DNA synapsis remains unclear. In eukaryotes, the Ku70/80 heterodimer

primarily acts as a DNA end-binding protein, recruiting additional NHEJ components for repair(13,14). Unlike its eukaryotic counterpart, mKu may play a more versatile role, potentially mediating synapsis independently or in collaboration with unknown partners. This presumed ability to align flexible DNA ends efficiently would distinguish mKu from other Ku proteins(8). Understanding the molecular mechanisms of mKu-mediated synapsis could offer unique insights into bacterial DNA repair and identify potential therapeutic targets.

Despite its biological importance, the structural and mechanistic basis of bacterial NHEJ remains poorly understood. Efforts to crystallize mKu have been hindered by the high flexibility of its C-terminal region, a trait observed in other bacterial Ku proteins such as *Bacillus subtilis* Ku(15). Additionally, mKu's tendency to oligomerize in the presence of linear DNA introduces structural heterogeneity, complicating crystallographic and other structural studies[8]. The small molecular size of mKu (31 kDa) poses further challenges for cryo-electron microscopy (cryo-EM), as resolving smaller proteins (<100 kDa) at high resolution remains difficult(16). Overcoming these challenges is essential for elucidating the molecular mechanisms underlying bacterial NHEJ and leveraging this knowledge for therapeutic development.

In this study, we employed cryo-EM to resolve the structure of mKu in complex with DNA, as well as to visualize the higher-order mKu-DNA oligomer (mKu-DNA supercomplex), which demonstrates novel mKu-mediated DNA synapsis. Using structural modeling and *in silico* alanine mutations, we identified critical residues for DNA binding and synapsis. We further explored the effects of DNA end modifications, such as hairpin structures, on the formation and stability of the DNA-protein complex and the supercomplex. Hydrogen-deuterium exchange mass spectrometry (HDX-MS) confirmed key interactions necessary for the formation of the mKu-DNA complex and synaptic assembly. Förster resonance energy transfer (FRET) was used to evaluate the stability and dynamics of the synaptic assembly in solution. Finally, live-cell imaging of *Mycobacterium smegmatis* fostering mKu (Mtb) allowed us to visualize and quantify the dynamic recruitment of mKu to DNA damage sites during the early stages of the NHEJ repair pathway.

Methods:

Recombinant protein expression and purification

The recombinant plasmid (pET16b) containing the gene expressing mKu (Rv0937c) was a generous gift from Prof. Aidan Doherty, University of Sussex(9). The mKu protein construct cloned under lactose inducible promoter was overexpressed with Isopropyl β-D-1-thiogalactopyranoside (IPTG) in *E.coli* BL21 (DE3) C43 strain. To obtain a homogenously purified protein sample affinity, ion exchange and size exclusion chromatography were performed in sequential order. The overexpression and detailed purification strategy have been reported in our previous publication(8). The purity of the isolated protein was accessed by the analytical size exclusion chromatography and SDS PAGE (Supplementary Figure 1).

Cryo-EM sample preparation and data collection

The DNA substrates were commercially synthesized with the following sequences: (i)) linear 40bp long double-stranded DNA (dsDNA): 5'-CCCCCCTGTCGCCGCCGACGTCTGTGAT ATGGCGTTGTTG-3' and 5'-CCCCCCTGTCGCCGCCGACGTCTGTGATATGGCGTTG TTG-3' (IDT). (ii) Short hairpin DNA (shDNA) with 21bp: 5'-GTTTTTAGTTTATTGGGCG CG-3' and 34bp: 5'-CGCGCCCAGCTTTCCCAGCTAATAAACTAAAAAC-3' (PDB:1JEY)(17). The DNA substrates were annealed by heating at 95º C followed by stepwise cooling to 4º C in a thermal cycler machine (ThermoFisher Scientific). The annealing buffer contained 10nM Tris pH 7.5, 50mM NaCl, and 1mM EDTA. The DNA substrates (dsDNA & shDNA) and mKu were incubated at an equimolar concentration of 5 µM for 30 mins at 4 ºC. The dimeric molecular weight of mKu (68kDa) was considered for molarity calculations as the protein is known to exist and function in the dimeric form. For grid preparation, 200 hole 1.2µm/1.3µm holey carbon grids (ProSciTech, cat# GCF200CU-1.2-25) were glow discharged (Quorum Technologies) at 15mA under vacuum for 3 mins. The longer than standard (30s) glow discharge time yielded better particle distribution. 4 µl of the sample were applied to the freshly glow discharged grids, which were blotted for 4 s at a blot force of 1 and plunge frozen in liquid ethane with a Vitrobot Mark IV (ThermoFisher Scientific) operated at 4 °C and 100% humidity. Following blotting and plunge freezing, the grids were clipped and loaded in a grid cassette for automated grid loading. Initial screening of grids was performed in Talos Arctica TEM (Thermo Fisher Scientific), followed by data acquisition in Titan Krios G4 (ThermoFisher Scientific) using the Falcon 4 detector. Movies were acquired at a magnification of x105,000 with a pixel size of 0.833 Å. For the mKu-dsDNA complex, a total

of 4,682 movies were collected at a total dose of 40 $e^-/Å^2$ spread equally over 40 frames. Movies were recorded over a defocus range of -1 to -2.5 µm. For the mKu-shDNA complex, a total of 6,151 movies were collected, and the data collection parameters were unchanged.

Cryo-EM processing and model building

Image processing and primary map generation was done using CryoSPARC v4.5.3(18). Motion correction and dose weighting were performed using the Patch Motion Correction job. Contrast Transfer Function (CTF) correction of the dataset was achieved with the Patch CTF job. Following the motion and CTF correction, the images were manually curated based on CTF fit resolution, ice thickness, and average intensity thresholds. Particle picking was initially done using the blob-picker with min and max diameters of 50 and 200 Å with an overlap of 0.5x diameter. Particle-picking parameters were adjusted, and different box sizes (256, 420 & 512 Å) were used to select and extract particles (mKu-DNA supercomplex) comprising 3 mKu dimers bound to 3 shDNA or 1.5 dsDNA molecules. As an alternate strategy, smaller box sizes (256 Å) were used to pick individual mKu_2-DNA complexes to later combine into a composite map. However, the resulting 2D classes (not reported) had lower quality due to a reduced signal-to-noise ratio caused by the small size of the mKu dimer (~70 Å in diameter). Thus, the particle picking was performed on the supercomplex rather than the unit mKu-DNA complex.

For the mKu-hairpin supercomplex, 1.15 million particles were primarily picked and extracted with a box size of 512 pixels, followed by 2D class averaging (100 classes) and manual curation to extract the unique orientations using a select 2D class job. Despite shDNA being shorter than dsDNA, mKu-shDNA oligomers had a higher curvature, requiring a larger extraction box to prevent loss of data (Supplementary Figures 2 & 3). The selected 2D classes were used as templates for template-based picking. Three rounds of 2D classification were done with manual curation between each cycle to obtain a final set of 229,557 particles. The resultant particles were used to generate *ab initio* maps using the Ab-initio reconstruction job in CryoSPARC. Three *ab initio* maps were generated with 43K, 110K, and 76K particles, respectively. Class II was selected for having the highest number of particles and better completeness in terms of 3D orientation. The *ab initio* maps were refined using the non-uniform refinement job, resulting in a global resolution (GSFSC 0.143) of 6.3, 6.8, and 4.1 Å (Supplementary Figure 4).

For the mKu-linear DNA supercomplex, the same workflow was used as above, with only the difference in the particle extraction box size (420 pixels). A total of 826,378K particles were

used for *ab initio* reconstruction. *Ab initio* maps were classified into three classes with 101K, 418K, and 306K particles. The non-uniform refinement of the generated classes resulted in the best global resolution (GSFSC 0.143) of 4.3, 3.9, and 3.8 Å (Supplementary Figure 4). Finally, the density maps of the super-complexes were improved via density modification using the Phenix Resolve CryoEM job(19) (Phenix)(20). The native maps were used to isolate the densities corresponding to unit mKu-DNA complexes by running a model-based density modification job (Phenix). The resultant dimensions of the EM maps were 111 x 115 x 99 pixels (mKu-shDNA) and 190 x 100 x 109 pixels (mKu-dsDNA).

The dimeric model of mKu was obtained from AlphaFold2(21). The model for linear DNA was obtained from our previous study(8) , and hairpin DNA was extracted from PDB: 1JEY(17). The atomic models were initially fitted (rigid body fitting) into the density-modified maps of the unit complexes with the Local EM fitting module from the Phenix bundle in ChimeraX. Once the unit complexes (linear and hairpin) were fitted into the map, additional copies of the mKu dimer and DNAs corresponding to the supercomplexes were added to the map using the Local EM fitting module in ChimeraX(22). Following the rigid body docking of the models to maps, iterative refinement was performed using Real-space refinement in Phenix. Outliers and atomic clashes were resolved manually in Coot(23), and simultaneous real-space refinements were performed in Phenix. Model quality was assessed using a rotamer, geometry, and density fit analysis in Coot. After the final refinement job, the local and global resolutions of the maps were determined by ResMap(24), Local resolution map (Phenix), 3DFSC (Cryosprac), and GSFSC (Cryosprac) (Supplementary Figure 4).

Hydrogen-deuterium exchange mass spectrometry

Hydrogen-deuterium exchange (HDX) labeling of the protein was conducted at 20°C. 3 µL aliquots of the purified protein (~15 µM, dimer) were added to 55 µl of either non-deuterated (50 mM potassium phosphate buffer, pH 7.4 in H_2O) or deuterated (50 mM potassium phosphate buffer, pH 7 in D_2O) buffer and incubated for 0, 0.1, 1, 10 and 100 mins using a PAL Dual Head HDX Automation Manager (Trajan/LEAP) controlled by ChronosHDX software. At the end of the incubation time, the reactions were quenched by mixing 50 µL of the deuterated protein sample with 50 µL of quenching buffer (50 mM potassium phosphate buffer, pH 2.3, 4 M guanidine hydrochloride, and 0.1% n-Dodecylphosphocholine) at 1°C.

For online pepsin digestion, 80 µL of the quenched samples were then passed through an immobilized Enzymate BEH pepsin column (2.1 × 30 mm; Waters), equilibrated in 0.1% formic acid at 100 µL/min. To reduce peptide carryover, 1% w/w n-Octyl-β-d-glucopyranoside was added to the column wash solution (1.5 M guanidine hydrochloride, 4% acetonitrile, 0.8% formic acid). The proteolyzed peptides were captured and desalted using a VanGuard BEH C18 trap column (1.7 µm, 2.1 × 5 mm; Waters), then eluted with a gradient of acetonitrile and 0.1% formic acid (5% to 40% over 8 minutes, 40% to 95% over 0.5 minutes, held at 95% for 1.5 minutes) at a flow rate of 80 µL/min, and separated on an ACQUITY UPLC BEH C18 analytical column (1.7 µm, 1 × 50 mm; Waters), delivered by an ACQUITY UPLC I-Class Binary Solvent Manager (Waters).

Mass spectrometry was performed using a SYNAPT G2-Si mass spectrometer (Waters) equipped with ion mobility. Instrument settings were as follows: 3.0 kV capillary voltage, 40 V sampling cone, source temperature at 100°C, and desolvation temperature at 40°C. The desolvation gas flow was set to 800 L/hr, and the cone gas flow was 100 L/hr. The high-energy trap collision energy was ramped from 20 to 40 V. Mass spectra were acquired with a 0.4-second scan time and continuous lock mass (Leu-Enk, 556.2771 m/z) for mass accuracy correction. Data were collected in HDMSE (ion mobility) mode, and peptides from non-deuterated samples were identified using Protein Lynx Global Server (PLGS) v3.0 (Waters). Peptide selection stringency was ensured by applying additional filters: 0.3 fragments per residue, minimum intensity of 5000, maximum MH+ error of 5 ppm, retention time RSD of 10%, and file threshold of 4 out of 6 HDMSE files. Deuterium uptake values were calculated for each peptide using DynamX 3.0 (Waters). Deuterium exchange experiments were conducted in triplicate for each time point. Peptides with statistically significant differences in HDX were identified using Deuteros 2.0 software (25), employing a hybrid significance test with a 99% confidence interval.

Förster Resonance Energy Transfer

Single-stranded DNA molecules were commercially synthesized (IDT) and annealed to get the blunt-ended dsDNA substrate. Individual DNA stands contained- Cy3 as a donor and Cy5 as an acceptor. The following sequences correspond to the two complementary strands of the DNA substrate: 5’Cy5/CCACACTGTCGCCGCCGACGTCTGTGATATGGCGTTGTTGCGCCG CCGAC/3’Cy3Sp and 5’Cy3/GTCGGCGGCGCAACAACGCCATATCACAGACGTCGGC

GGCGACAGTGTGG/3'Cy5Sp to have a donor and acceptor fluorophores at opposite ends. The fluorescence signal was detected at $\lambda_{excitation}$ of 554 nm (λ_{ex} of Cy3) and $\lambda_{emission}$ of 670 nm (λ_{em} of Cy5) using Cary Eclipse Fluorescence Spectrometer (Agilent). The negative control set with no mKu was prepared with 250nM DNA in 10 mM PBS buffer pH 7.4. Buffer control was used as blank to remove the background signal from the buffer. For the FRET assay, a fixed concentration of 250 nM DNA solution was titrated with increasing concentrations of mKu (0-305 nM) until the fluorescence emission signal reached saturation. Incubation time between injection and data acquisition was kept constant at 1 min. The experiment was performed in triplicates at 25 ºC using a Peltier system attached to the Spectro fluorimeter. Wave scans (emission: 570-700nm) were performed for respective mKu concentrations to quantify the fluorescence intensities at $\lambda_{emission}$ maximum (Supplementary Figure 7). Finally, the normalized fluorescence intensities (λ_{max}) corresponding to respective concentration mKu were graphically represented (Fig 5.e).

Live cell confocal microscopy

Mycobacterium smegmatis mc^2 155 *Δku ΔligD* strain(26) (Mgm 153) was a kind gift from Prof. Michael S. Glickman, Memorial Sloan Kettering Cancer Center, New York. The modified *M.smegmatis* stain (Mgm 153) is NHEJ impaired with the intrinsic *ku* and *ligD* genes deleted. Cells were cultured in Middlebrook 7H9 media with 0.5% dextrose, 0.5% glycerol, and 0.05% Tween 80. The liquid media was fortified with the OADC supplement (oleic acid, bovine albumin, sodium chloride, dextrose, and catalase), along with 100 µg/ml ampicillin, to avoid bacterial contamination. Where applicable, 50 µg/ml hygromycin B was used. The plasmid pYUB1062-GFP(27) (Plasmid #117695, Addgene) was used to synthesize the mKu-GFP fusion construct (Genscript). The recombinant plasmid was electroporated in electro-competent Mgm 153 cells using a MicroPulser electroporator (Biorad) with one pulse at 2.5kV. For electroporation, the EC2 (company-recommended) setting was used in a 0.2 cm cuvette. The cells were revived in Middlebrook 7H9 media and grown in Middlebrook 7H10 agar with hygromycin B for 72 hours. For imaging, mKu-GFP transfected Mgm 153, and Mgm153 control cells were grown in liquid media until the OD_{260} reached 0.6. The cells were induced with 0.2% acetamide and incubated at 37 ºC for 20 hours. Finally, 1 ml of cells were harvested and incubated with 0.5% v/v Hoechst 33342 (ThermoFisher) for 30 minutes. The stained cell suspension was overlaid onto a 1% agarose pad on a glass slide and maintained at 37°C in a temperature and humidity-controlled chamber. Fluorescence imaging was performed using a

Zeiss LSM900 inverted confocal microscope equipped with an Airyscan 2 detector and a 63× oil immersion objective (working distance: 140 µm). Images were acquired in laser scanning confocal mode. Each acquisition consisted of 70 image stacks captured at 5.65 second intervals. To induce laser-mediated DNA damage, a 405 nm laser was targeted at a region of interest (ROI) of 1.0 × 0.8 µm. Damage was introduced after the third frame (after 11.30 sec), with the first three frames (0 – 11.30 sec) serving as pre-damage snapshots and frames 4 to 70 (16.96 – 300 sec) capturing post-damage responses. For the control set, no laser damage was introduced with the dimension of ROIs, and image acquisition parameters remained unaltered. DNA was visualized using the DAPI channel at the detection range of 400-500nm, while GFP-tagged mKu was visualized using the GFP channel at the detection range of 495-600 nm. The image stacks were processed in FIJI(28). The time-dependent fluctuation of DAPI and GFP intensities at the ROI was analyzed using the plot Z-axis profile function in FIJI. The data statistics and normalizations were performed in Origin(Pro), Version 2024.

Results:

Mycobacterial Ku homodimers form higher order oligomers in complex with linear and short hairpin DNA molecules

Our previous study demonstrated that mycobacterial Ku (mKu) forms higher-order oligomers in the presence of DNA(8). These oligomeric complexes were obtained using chemically synthesized 40 base pairs long linear dsDNA molecule. However, the resultant complexes were of heterogeneous lengths, measuring more than 200 nm, corresponding to several dozens of mKu dimers (~6 nm each) adjacently placed, forming a filamentous structure (Supplementary Figure 2).

In an attempt to obtain structurally homogenous complexes of DNA and mKu, we assembled DNA-mKu complexes using a hairpin-DNA molecule inspired by the human Ku70/80-DNA complex crystal structure (PDB: 1JEY). This structure used a short-hairpin DNA (shDNA) comprising a 34-mer and a 21-mer ssDNA, annealed to form dsDNA with a hairpin at one terminus. We predicted that the bulky terminal hairpin would prevent mKu from forming higher-order oligomers. However, contrary to our expectations, we observed long filamentous oligomers (Supplementary Figure 2) approximately 6 nm in diameter and ~50-100 nm in length rather than well-defined or discrete particles formed by a mKu dimer and DNA. The mKu-shDNA particles were shorter with more curvature than those obtained with dsDNA, indicating

that the bulky hairpin inflicted some hindrance in the system but was insufficient to prevent assembly into filaments (Supplementary Figure 2).

Cryo-EM structures of mKu homodimer in complex with dsDNA and shDNA molecules

To determine the structure of the supercomplex mKu bound to DNA, 5 μM of the purified mKu dimer was incubated with an equimolar concentration of dsDNA or shDNA. The 3D reconstruction was performed using the single-particle cryo-EM image analysis with box sizes encompassing 3 mKu dimers and 1.5 dsDNA molecules or 3 shDNA. This box sizes were chosen based on a series of 2D classifications.

Our maps had a GSFSC (gold-standard Fourier shell correlation) resolution of 3.8 Å for dsDNA and 4.1 Å for shDNA. The resolutions of these maps were sufficient to enable us to build several models (Figure 1). The data collection, validation, and refinement statistics are provided in Supplementary Table 1. The cryoEM workflow, map validation, and resolution estimation are presented in Supplementary Figures 3 & 4. These maps showed clearly defined densities for the Ku dimers and the DNA spanning the dimers. Each Ku dimer has an approximately triangular prism 3D shape with a hole at the top of its lateral face through which DNA molecules are threaded. The two Ku molecules are highly intertwined within the dimer. The Ku dimers interact extensively at the bottom of their lateral faces at a defined angle, forming a continuous protein filament. However, the flexible C-terminal tail of mKu could not be traced on the EM map because of the lack of corresponding density. The Continuous densities for the DNA molecules are resolved in the EM maps, with the major and minor grooves of the DNA clearly visible. The DNA molecules are better resolved in the linear DNA density map and are positioned end-to-end along the central axis of the Ku filament. Continuous density for DNA is also present in the EM map. The density in the shDNA was less resolved with no density was observed for the hairpin itself, suggests that adjacent shDNA molecules were in close proximity but in an energetically unfavourable arrangement, possibly due to hindrance from the bulky hairpin moiety.

Molecular hand-clenching facilitates mKu dimerization

Mycobacterial Ku is a dimer in solution and partially resistant to SDS(8). The melting temperature of the dimer is 50° C, which is considerably high for a protein in its apo state(8). Our models of mKu dimer (PDB: 8V53,8VF5) reveal that the interaction between the two

monomers of mKu resembles two human hands clenched together (Figure 2. a, b). The regions of contact in the dimeric interface are broadly divided as (i) the bridge (residue: 23-91), (ii) the pillar (α-helix-#4), and (iii) the sling (residue: 167-227) comprising a helix-turn-helix (HTH) motif (Figure 2.c). The **bridge** comprises three beta-hairpins (ß2 – ß4) in antiparallel contact with the opposite monomer, mimicking crisscrossed human fingers (numbered 1-3, shown in Figure 2). Building on the observations from EM structures, HDX-MS revealed that β-hairpins 2 and 3 were protected from deuterium-to-hydrogen exchange (Figure 3. a, b). Such protection in HDX-MS indicates that these regions are involved in interactions, with the residues being either fully or partially buried within the protein dimer. Our models suggest total of 20 H-bonded contacts and two salt bridges (Ku1-E65:R30-Ku2 & Ku2-E65:H32-Ku1) interactions in the bridge region, as calculated from the dimer structure using LigPlot+ (Supplementary Figure 5). The **pillar** and β-hairpin4 of Ku1 form a cleft that houses Ku2 β-hairpin2 via non-bonded contacts (Figure 2. c. ii). Finally, the **sling** arises from two respective monomers and wraps around the whole complex in opposite directions, enhancing the compactness of the dimer. The sling forms significant contact with the β-barrel of the opposite monomer (Figure 2.c.iii). Overall, these three interfaces (bridge, pillar & sling) contribute to the relative rigidity and stability of the mKu dimer.

Identification and cross-validation of critical residues in mKu-DNA complex

Ku homodimer interacts with the DNA via the central pore located at the center of the dimer. The DNA binding pore is lined with positively charged residues (Supplementary Fig .6), perfectly suitable for a sequence non-specific interaction with the sugar-phosphate backbone of a dsDNA molecule. In the mKu-DNA complex, the DNA acts like a nut, sliding into the DNA binding pore of mKu, similarly resembling a bolt. This mode of nut-bolt assembly of Ku and DNA is conserved across species(7). However, the functional aspects of Ku vary in lower and higher organisms due to the presence or absence of additional domains at the N and C termini of the protein(7).

The DNA-mKu interaction is mediated majorly by positively charged residues (Arg & Lys) of the mKu dimer and the negatively charged sugar-phosphate backbone of the DNA (Figure 4). mKu interacts with the DNA at two distinct regions on the DNA, at the DNA termini (End) and the central area of the DNA (Mid) encompassed by the bridge region of mKu (Figure 4). The residue-specific contacts are mapped in a 2D figure for better visualization (Figure 4.b).

Residues Y(21 & 44), Q33, and R(43,44,46,58,62 & 88) were found to form H-bonded contacts with the backbone of the DNA double-helix (Figure 4.b). Similarly, the stretch of interacting residues lining the DNA binding pore was found protected in HDX-MS (Figure 3.a, b). In addition to the H-bonded contacts, several non-bonded contacts stabilize the DNA-Ku complex. Overall, the tight binding of the DNA at the positively charged pore of mKu explains the previously reported high thermal stability of the mKu-DNA complex (Tm = 70º C)(8).

To identify the critical residues for DNA binding, we performed *in-silico* alanine mutation of the interacting residues and assessed the mutants' stability compared to the wild type. Mutations of Y21 and R(58 & 88) destabilized the DNA protein complex (Supplementary Table 4). Meanwhile, mutations of Y44, Q33, and R(43,44,46,62) were highly destabilizing (Supplementary Table 4). AlphaFold3 predictions of the mKu-DNA complex with site-specific alanine mutations showed a loss of the native positively charged lining in the DNA-binding pore, leaving the DNA molecule partially lodged within the pore.

Higher order oligomerization of mKu directs DNA synapsis

DNA end binding of Ku has been proposed to be the rate-limiting step in NHEJ(6). Our data suggests that mycobacterial Ku has a critical role in initiating the DSB repair. In addition to DNA binding and protecting broken DNA ends from exonucleases(8), mycobacterial Ku independently facilitates DNA synapsis via mKu dimer oligomerization (PDB: 8VF2, 8VF4). The mKu-mediated synapsis is formed by the simultaneous association of the mKu dimer-1 (chain A & B) bound to DNA1 (chains E & F) with an adjacent mKu dimer-2 (chain C & D) bound to DNA2 (chains G & H). The DNA-mKu interactions are discussed in detail in the preceding section. In the mKu1-mKu2 super-complex interface, we found that ß-hairpin1 from the adjacent mKu dimers make hydrogen-bonded and non-bonded contacts. Specifically, residues 12 to 15 (GLVN) present in the ß-turn region of the ß-hairpin1 motif were found to interact with the ß-hairpin1 motif of the adjacent mKu dimer (mKu2) and the surrounding helix-3 and 4 (Figure 5). The helix 3 and 4 from the adjacent mKu dimers (mKu1 & 2) create a four-helix pocket that creates and stabilizes the aforementioned super-complex interface. The following H-bonded contacts were observed between ß-hairpin1 and helix 3,4: mKu1-B-12-Gly to mKu2-C-191-Glu (Bond distance: 2.97 Å), mKu1-B-118-Ser to mKu2-D-15-Asn (Bond distance: 2.08 Å), mKu1-B-121-Ser to mKu2-D-13-Leu (Bond distance: 2.77 Å). Here, the residues are annotated as Dimer ID-Chain ID-Residue Number-Residue Name. To assess the

contribution of the residues mentioned above in ß-hairpin1, we have modeled the mutants of mKu using AlphaFold3. We found that the deletion mutants- mKuΔ12-15 and mKuΔ1-15- resulted in complete disorientation and disassembly of the synaptic complex (Figure 5.d & Supplementary Table 5). In contrast, alanine substitution of 12-15 did not impact the complex assembly.

Unlike eukaryotic Ku, mKu can form a DNA synapse independently. We cross-validated this unique ability of mKu by complementing cryo-EM data with Förster resonance energy transfer (FRET) and hydrogen-deuterium exchange mass spectrometry (HDX-MS). Solution-based assays like FRET and HDX-MS evaluate the stability and kinetics of the synapse, which structure determination techniques may not clearly establish. For the FRET assay, DNA concentration was held constant while the mKu protein was titrated to saturation (Figure 5.e). As mKu concentration increased, the donor emission signal gradually decreased, accompanied by a simultaneous increase of the acceptor signal, indicating FRET between the donor and acceptor fluorophores. The DNA synapse remained consistently stable at 25°C during the experiment. These findings demonstrate that mKu is sufficient to form stable DNA synapsis on blunt-ended dsDNA substrates.

Further, we evaluated the synaptic complex's stability and kinetics via HDX-MS over 0 to 100 mins. The interactions that were identified from the structure as pivotal for the DNA synapsis (ß1 and helix-3,4) were found to be protected at 0.1 to 100mins. This indicates stable contact at the interface region, reflected by relatively lower deuterium uptake. Uptake plots for the residues critical for synapsis are presented separately (Fig 3. f). The HDX-MS data statistics are shown in Supplementary Table 2.

Capturing the initial phases of Mycobacterial NHEJ repair

To study the localization and dynamics of mKu following DNA damage, we visualized *M. smegmatis* (*Ku*$^{-}$ *LigD*$^{-}$) cells lacking the NHEJ apparatus complemented with inducible plasmids carrying mKu-GFP. Laser-induced DNA damage at an area of 0.8 µm x 1µm resulted in an instantaneous influx of the mKu-GFP to the damaged foci (Figure 7). The intensity gradually dissipated with time, likely due to mKu sliding on the DNA molecules(8). The image acquisition was performed before and after photobleaching to compare the localization of mKu-GFP at the respective states. In the control ROI without damage, mKu-GFP was well-dispersed throughout the cell, similar to pre-photobleaching observations. Quantifying

intensity fluctuations in the laser-bleached ROI showed a simultaneous spike in the green channel, corresponding to mKu-GFP, and a sharp drop in the DAPI channel due to photobleaching (Figure 7.b). These observations suggest that mKu functions as a molecular switch acting as a double-strand break (DSB) reporter.

Discussion:

The findings of this study significantly advance the understanding of the non-homologous end-joining (NHEJ) DNA repair mechanism in prokaryotic systems, focusing on *Mycobacterium tuberculosis* (Mtb). This research explored the structural and functional properties of the mycobacterial DNA-binding protein Ku (mKu) and its active role in DNA repair and synapsis. Following a DNA double-stranded break, mKu sequentially stabilizes broken DNA strands(8), protects them from exonucleases(8), facilitates DNA synapsis formation, and accommodates the DNA ligase(29)—all without requiring cofactors or accessory partners, unlike the eukaryotic NHEJ machinery(11). Building on prior studies, this work elucidates mKu's dimerization, its DNA association, and the novel mKu-mediated synapsis of broken DNA strands, processes essential for effective double-stranded break repair (DSBR). By combining cutting-edge techniques such as cryo-electron microscopy (cryo-EM), hydrogen-deuterium exchange mass spectrometry (HDX-MS), and live-cell imaging, this research adds a new dimension to the understanding of prokaryotic NHEJ repair systems, highlighting the distinctiveness of mKu in maintaining the genomic stability of Mtb.

Cryo-EM reconstructions provided detailed structural insights into mKu complexes with double-stranded DNA (dsDNA) and hairpin DNA (shDNA) at 3.8 Å and 4.1 Å resolution, respectively. The findings confirmed that mKu engages DNA via a positively charged pore, forming a nut-bolt assembly similar to its eukaryotic counterpart. However, unlike human Ku, mKu independently mediates stable DNA synapsis through higher-order oligomerization, reflecting a mechanistic divergence potentially tailored to prokaryotic adaptations. The super-complex structures revealed continuous DNA density in the linear DNA EM map, suggesting stable end-to-end DNA arrangements mediated by mKu oligomers. In contrast, the reduced resolution and lack of density for hairpin DNA in shDNA complexes indicate potential conformational flexibility due to terminal hairpins. These findings highlight mKu's adaptability to DNA modifications via modulation of the helical twist at its synaptic interface. FRET-based assays with longer dsDNA (60 base pairs) confirmed stable and independent mKu-mediated DNA synapsis in solution.

Positively charged residues at the DNA-binding interface (R43, R44, R46, R58, R62, and R88) underscore charge-complementary interactions crucial for mKu's robust DNA association and high thermal stability. Covalent interactions with the sugar-phosphate backbone explain the sequence non-specificity in DNA binding. Kinetic HDX-MS studies of mKu-dsDNA and mKu-shDNA complexes confirmed the persistent burial of the DNA-binding pore over 100 minutes, indicating a universal and robust DNA-binding mode. *In silico* alanine substitutions at interface residues destabilized the mKu-DNA complex, potentially impairing DNA binding and super-complex stability, underscoring their importance. Future experiments, such as electrophoretic mobility shift assays (EMSA) or surface plasmon resonance (SPR), are needed to validate these observations and quantify their effects in detail. The conserved nut-bolt assembly of Ku-DNA complexes, coupled with mKu's thermal stability, illustrates Ku proteins' evolutionary conservation and adaptation in prokaryotic repair systems.

The unique ability of mKu to mediate DNA synapsis independently through oligomerization showcases a distinct functional advantage in prokaryotic NHEJ. Structural analysis revealed β-hairpin-mediated interactions at the synaptic interface, with residues 12–15 (GLVN) forming key contacts with adjacent mKu dimers. Deletion of these residues disrupted synaptic complexes *in silico*, highlighting their importance in stabilizing DNA synapsis and maintaining super-complex integrity. The instability of the DNA synapse would severely impair the pathogen's NHEJ machinery. Experimental validation of these deletions *in vitro* could provide concrete evidence and open avenues for targeted drug discovery. These findings underscore a unique adaptation of mycobacterial NHEJ, potentially exploitable for therapeutic interventions against persistent Mtb infections.

Interestingly, mKu exists as a homodimer in solution and oligomerizes solely upon binding linear DNA. The homodimer resembles two human hands clenched together, stabilized by β-hairpin interactions and a helix-turn-helix motif, which add compactness. Despite this compact arrangement, the C-terminal region (CTR, residues 228–273) is highly flexible, as evidenced by its missing density in cryo-EM structures and deprotected nature in HDX-MS. This flexibility likely facilitates CTR in capturing and housing DNA ligase (ligD) at synaptic foci(29). Binding to ligD may reduce the flexibility of of mKu's CTR, enhancing super-complex stability.

Live-cell confocal imaging of *Mycobacterium smegmatis* cells expressing mKu-GFP revealed the cellular distribution of mKu and its rapid influx to the sites of laser-induced DNA damage.

This influx, driven by mKu's high affinity for linear DNA (0.33 nM)(8), supports its role as a damage sensor. As mKu binds to the DNA ends, it gradually slides along the strand to recruit additional dimers, as observed in cryo-EM micrographs. However, given the extensive size of Mtb's genomic DNA (4.4 Mbp), the abundance of mKu within the cell may be insufficient to span such lengths. Future studies should assess mKu's coverage capacity on native genomic DNA.

This study offers novel insights into prokaryotic two-component DNA repair systems, emphasizing the pivotal role of mKu as a rate-limiting factor. It presents the first report of Ku-mediated DNA synapsis and explores its implications for disrupting Mtb's NHEJ repair system. Future research could investigate the irreversibility of mKu-DNA complexes post-NHEJ and evaluate the role of other repair factors in regulating prokaryotic NHEJ. Real-time imaging of the two-component NHEJ repair apparatus will provide invaluable insights into the spatiotemporal dynamics of DSB repair in Mtb, potentially informing strategies for targeted therapeutic interventions.

Conclusion:

The presented research advances our understanding of the non-homologous end-joining (NHEJ) DNA repair mechanism in *Mycobacterium tuberculosis* (Mtb) by uncovering the structural and functional dynamics of the mycobacterial Ku protein (mKu). Unlike eukaryotic NHEJ systems, mKu operates autonomously to stabilize DNA ends, mediate synapsis, and facilitate ligase recruitment, providing a unique perspective on prokaryotic DNA repair. Through cutting-edge techniques such as cryo-electron microscopy (cryo-EM), hydrogen-deuterium exchange mass spectrometry (HDX-MS), and live-cell imaging, this work delineates mKu's capacity for sequence-independent DNA binding, synaptic stabilization, and oligomerization into higher-order complexes, which are critical for genomic integrity in Mtb.

Data availability:

For ds-DNA and sh-DNA, the cryo-EM density maps have been deposited in the Electron Microscopy Data Bank (EMDB) under IDs EMD- 43184, -43186 and EMD- 42978, -43185, respectively. Coordinates are deposited in the Protein Data Bank (PDB) under IDs PDB- 8VF5, 8VF2, and 8V53, 8VF4, respectively. The HDX-MS data are available from ProteomeXchange via the PRIDE partner repository with the identifier PXD060776.

Author contributions:

J.B. conceptualized the study and conducted biochemical and biophysical experiments, light microscopy and cryo-EM sample preparation, cryo-EM data processing, single-particle 3D reconstruction, and model building under the guidance of E.H., A.K.D., and I.R. C.S.A. collected HDX-MS data, which J.B. analyzed under C.S.A.'s supervision. K.S. and J.B. collected light microscopy data, with J.B. processing and analyzing it under the supervision of P.J.M. and E.H. J.B. and I.R. wrote the manuscript with contributions from all authors.

Acknowledgments:

We sincerely thank the University of Melbourne's research platforms, including the Ian Holmes Imaging Centre (IHC) for access to the Cryo-EM platform, the Biological Optical Microscopy Platform (BOMP) for light microscopy facilities, the Mass Spectrometry and Proteomics Facility for HDX-MS data collection, and the Melbourne Protein Characterisation (MPC) Facility for support with protein purification and characterization. We are especially grateful to Dr. Hamish Brown and Dr. Sepideh Valimehr (IHC) for their assistance with electron microscopy training and data collection and to Dr. Mohammad Hossein Tanipour for his guidance on EM grid preparation. We also acknowledge Martin Fleming for technical support and Sean Crosby for supercomputing assistance. Data storage and processing were conducted in the Rouiller lab and on the Spartan supercomputer hosted by Melbourne Research Computing. We thank Prof. Aidan Doherty (University of Sussex) for providing the mKu-containing recombinant plasmid (pET16b-mKu) and Prof. Michael S. Glickman (Memorial Sloan Kettering Cancer Center, New York) for the *Mycobacterium smegmatis* mc² 155 Δku ΔligD strain (Msm 153). We acknowledge the Melbourne India Postgraduate Academy (MIPA) program for facilitating the joint collaboration and doctoral degree program (granted to JB) between IIT Kharagpur and the University of Melbourne.

Funding Information:

The research was supported by the National Health and Medical Research Council (NHMRC) Ideas Grant (APP2000934) and the Australian Government (awarded to IR), as well as the Science and Engineering Research Board (SERB), Government of India (Core Research Grant DST No. CRG/2020/002622, awarded to AKD).

Conflict of Interest: None

Reference:

1. Cannan, W.J. and Pederson, D.S. (2016) Mechanisms and Consequences of Double-Strand DNA Break Formation in Chromatin. *J Cell Physiol*, **231**, 3-14.
2. Salina, E.G. and Makarov, V. (2022) Mycobacterium tuberculosis Dormancy: How to Fight a Hidden Danger. *Microorganisms*, **10**, 2334.
3. Gong, C., Bongiorno, P., Martins, A., Stephanou, N.C., Zhu, H., Shuman, S. and Glickman, M.S. (2005) Mechanism of nonhomologous end-joining in mycobacteria: a low-fidelity repair system driven by Ku, ligase D and ligase C. *Nat Struct Mol Biol*, **12**, 304-312.
4. Pitcher, R.S., Green, A.J., Brzostek, A., Korycka-Machala, M., Dziadek, J. and Doherty, A.J. (2007) NHEJ protects mycobacteria in stationary phase against the harmful effects of desiccation. *DNA Repair (Amst)*, **6**, 1271-1276.
5. Amarh, V. and Arthur, P.K. (2019) DNA double-strand break formation and repair as targets for novel antibiotic combination chemotherapy. *Future Sci OA*, **5**, Fso411.
6. Della, M., Palmbos, P.L., Tseng, H.M., Tonkin, L.M., Daley, J.M., Topper, L.M., Pitcher, R.S., Tomkinson, A.E., Wilson, T.E. and Doherty, A.J. (2004) Mycobacterial Ku and ligase proteins constitute a two-component NHEJ repair machine. *Science*, **306**, 683-685.
7. Pitcher, R.S., Brissett, N.C. and Doherty, A.J. (2007) Nonhomologous end-joining in bacteria: a microbial perspective. *Annu Rev Microbiol*, **61**, 259-282.
8. Baral, J., Bhattacharje, G., Dash, S., Samanta, D., Hinde, E., Rouiller, I. and Das, A.K. (2024) In silico and in vitro characterization of the mycobacterial protein Ku to unravel its role in non-homologous end-joining DNA repair. *International Journal of Biological Macromolecules*, **278**, 134584.
9. Weller, G.R., Kysela, B., Roy, R., Tonkin, L.M., Scanlan, E., Della, M., Devine, S.K., Day, J.P., Wilkinson, A., d'Adda di Fagagna, F. *et al.* (2002) Identification of a DNA nonhomologous end-joining complex in bacteria. *Science*, **297**, 1686-1689.
10. Zhao, B., Rothenberg, E., Ramsden, D.A. and Lieber, M.R. (2020) The molecular basis and disease relevance of non-homologous DNA end joining. *Nature Reviews Molecular Cell Biology*, **21**, 765-781.
11. Chen, S., Lee, L., Naila, T., Fishbain, S., Wang, A., Tomkinson, A.E., Lees-Miller, S.P. and He, Y. (2021) Structural basis of long-range to short-range synaptic transition in NHEJ. *Nature*, **593**, 294-298.
12. Öz, R., Wang, J.L., Guerois, R., Goyal, G., KK, S., Ropars, V., Sharma, R., Koca, F., Charbonnier, J.-B., Modesti, M. *et al.* (2021) Dynamics of Ku and bacterial non-homologous end-joining characterized using single DNA molecule analysis. *Nucleic Acids Research*, **49**, 2629-2641.
13. Graham, T.G., Walter, J.C. and Loparo, J.J. (2016) Two-Stage Synapsis of DNA Ends during Non-homologous End Joining. *Mol Cell*, **61**, 850-858.
14. Stinson, B.M. and Loparo, J.J. (2021) Repair of DNA Double-Strand Breaks by the Nonhomologous End Joining Pathway. *Annu Rev Biochem*, **90**, 137-164.
15. McGovern, S., Baconnais, S., Roblin, P., Nicolas, P., Drevet, P., Simonson, H., Piétrement, O., Charbonnier, J.-B., Le Cam, E., Noirot, P. *et al.* (2016) C-terminal region of bacterial Ku controls DNA bridging, DNA threading and recruitment of DNA ligase D for double strand breaks repair. *Nucleic Acids Research*, **44**, 4785-4806.

16. Wu, M. and Lander, G.C. (2020) How low can we go? Structure determination of small biological complexes using single-particle cryo-EM. *Curr Opin Struct Biol*, **64**, 9-16.
17. Walker, J.R., Corpina, R.A. and Goldberg, J. (2001) Structure of the Ku heterodimer bound to DNA and its implications for double-strand break repair. *Nature*, **412**, 607-614.
18. Punjani, A., Rubinstein, J.L., Fleet, D.J. and Brubaker, M.A. (2017) cryoSPARC: algorithms for rapid unsupervised cryo-EM structure determination. *Nature Methods*, **14**, 290-296.
19. Terwilliger, T.C., Ludtke, S.J., Read, R.J., Adams, P.D. and Afonine, P.V. (2020) Improvement of cryo-EM maps by density modification. *Nature Methods*, **17**, 923-927.
20. Liebschner, D., Afonine, P.V., Baker, M.L., Bunkoczi, G., Chen, V.B., Croll, T.I., Hintze, B., Hung, L.W., Jain, S., McCoy, A.J. *et al.* (2019) Macromolecular structure determination using X-rays, neutrons and electrons: recent developments in Phenix. *Acta Crystallogr D Struct Biol*, **75**, 861-877.
21. Yang, Z., Zeng, X., Zhao, Y. and Chen, R. (2023) AlphaFold2 and its applications in the fields of biology and medicine. *Signal Transduction and Targeted Therapy*, **8**, 115.
22. Meng, E.C., Goddard, T.D., Pettersen, E.F., Couch, G.S., Pearson, Z.J., Morris, J.H. and Ferrin, T.E. (2023) UCSF ChimeraX: Tools for structure building and analysis. *Protein Science*, **32**, e4792.
23. Emsley, P. and Cowtan, K. (2004) Coot: model-building tools for molecular graphics. *Acta Crystallogr D Biol Crystallogr*, **60**, 2126-2132.
24. Kucukelbir, A., Sigworth, F.J. and Tagare, H.D. (2014) Quantifying the local resolution of cryo-EM density maps. *Nature Methods*, **11**, 63-65.
25. Lau, A.M., Claesen, J., Hansen, K. and Politis, A. (2021) Deuteros 2.0: peptide-level significance testing of data from hydrogen deuterium exchange mass spectrometry. *Bioinformatics*, **37**, 270-272.
26. Stephanou, N.C., Gao, F., Bongiorno, P., Ehrt, S., Schnappinger, D., Shuman, S. and Glickman, M.S. (2007) Mycobacterial nonhomologous end joining mediates mutagenic repair of chromosomal double-strand DNA breaks. *J Bacteriol*, **189**, 5237-5246.
27. Radhakrishnan, A., Furze, C.M., Ahangar, M.S. and Fullam, E. (2018) A GFP-strategy for efficient recombinant protein overexpression and purification in Mycobacterium smegmatis. *RSC Adv*, **8**, 33087-33095.
28. Schindelin, J., Arganda-Carreras, I., Frise, E., Kaynig, V., Longair, M., Pietzsch, T., Preibisch, S., Rueden, C., Saalfeld, S., Schmid, B. *et al.* (2012) Fiji: an open-source platform for biological-image analysis. *Nature Methods*, **9**, 676-682.
29. Sowa, D.J., Warner, M.M., Tetenych, A., Koechlin, L., Balari, P., Rascon Perez, J.P., Caba, C. and Andres, S.N. (2022) The Mycobacterium tuberculosis Ku C-terminus is a multi-purpose arm for binding DNA and LigD and stimulating ligation. *Nucleic Acids Res*, **50**, 11040-11057.

Figures:

Figure 1 | Cryo-EM structure of prokaryotic Ku homodimer-DNA supercomplexes

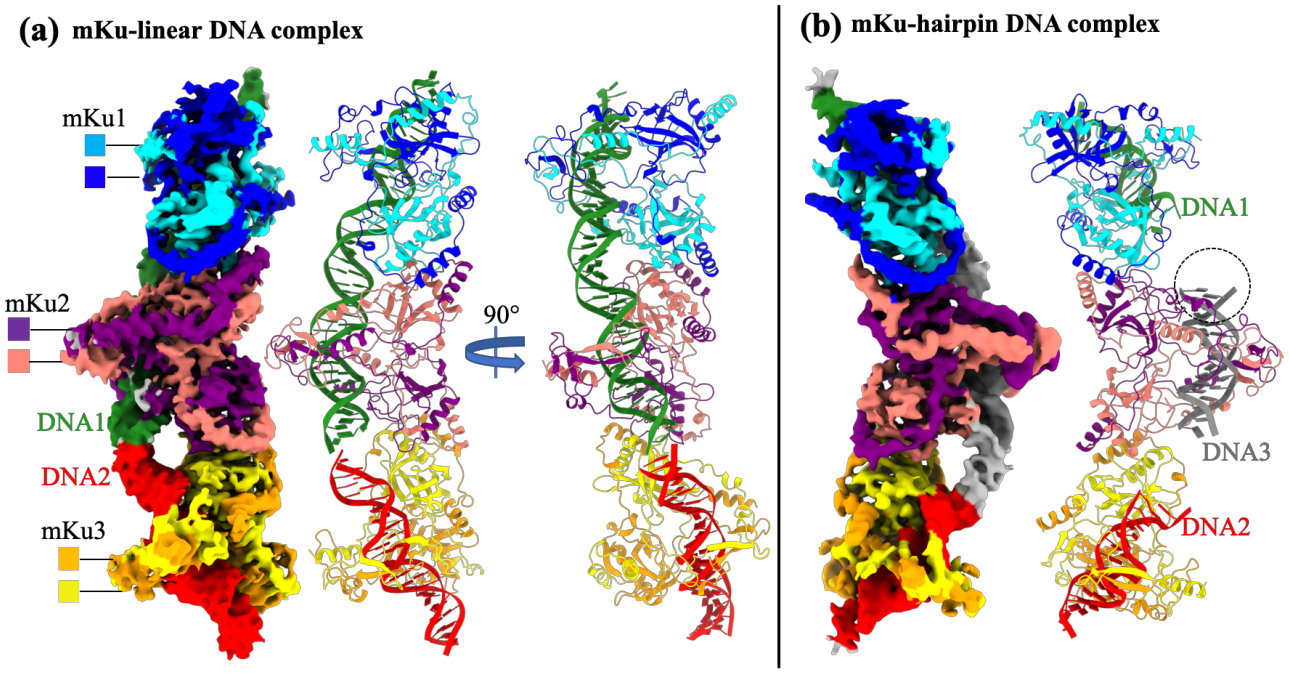

Figure 1 | Cryo-EM structures of the prokaryotic Ku-DNA complex: (a) EM map and structural model of the mKu-linear DNA supercomplex. Three adjacent mKu dimers are bound to two linear DNA molecules, with each protein and DNA chain colour-coded as shown. The C-terminal 46 residues of the mKu protein are not visible due to missing electron density. (b) EM map and structural model of the mKu-hairpin DNA supercomplex. Three adjacent mKu dimers are bound to three DNA molecules, having a terminal hairpin. The hairpin region (dotted circle) is unresolved due to missing electron density.

Figure 2 | Hand clenching dimeric association of mKu imparts compactness and stability

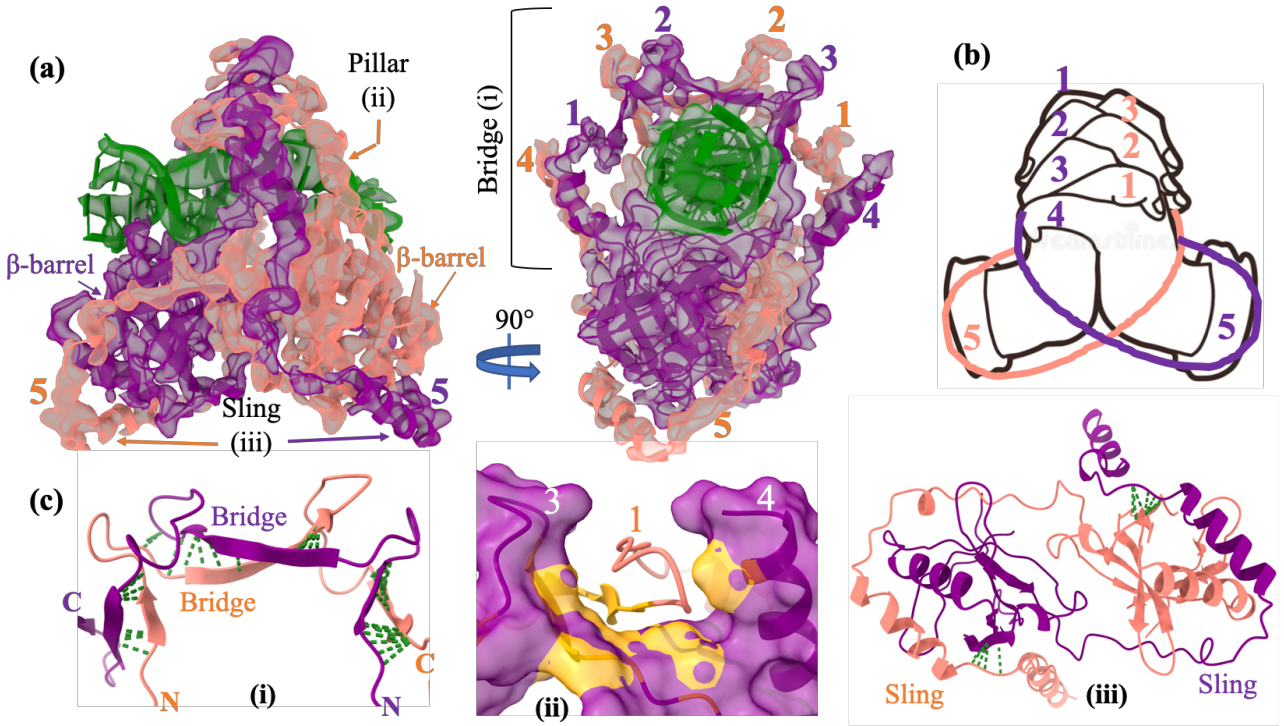

Figure 2 | Molecular hand-clenching of mKu homodimer: (a) EM map with the overlaid model showing two mKu monomers (coloured purple and salmon) interacting through three regions: (i) Bridge (1–3), (ii) Pillar (4), and (iii) Sling HTH motif (5). The numeric notations (1–5) denote the contact regions and do not indicate the

protein's secondary structural features, such as β-hairpins or helices. (b) A schematic representation highlights the resemblance between the mKu dimer and clenched human hands, where the fingers correspond to the contact regions (1–5). The outline image of human hands was obtained from Deamstime.com (c) Detailed views of the mKu dimer interfaces (i, ii, and iii). For clarity, the dimeric complex is truncated to enhance visualization. Green dotted lines represent the contact points.

Figure 3 | Assessing protein-protein and DNA-protein contacts by HDX-MS

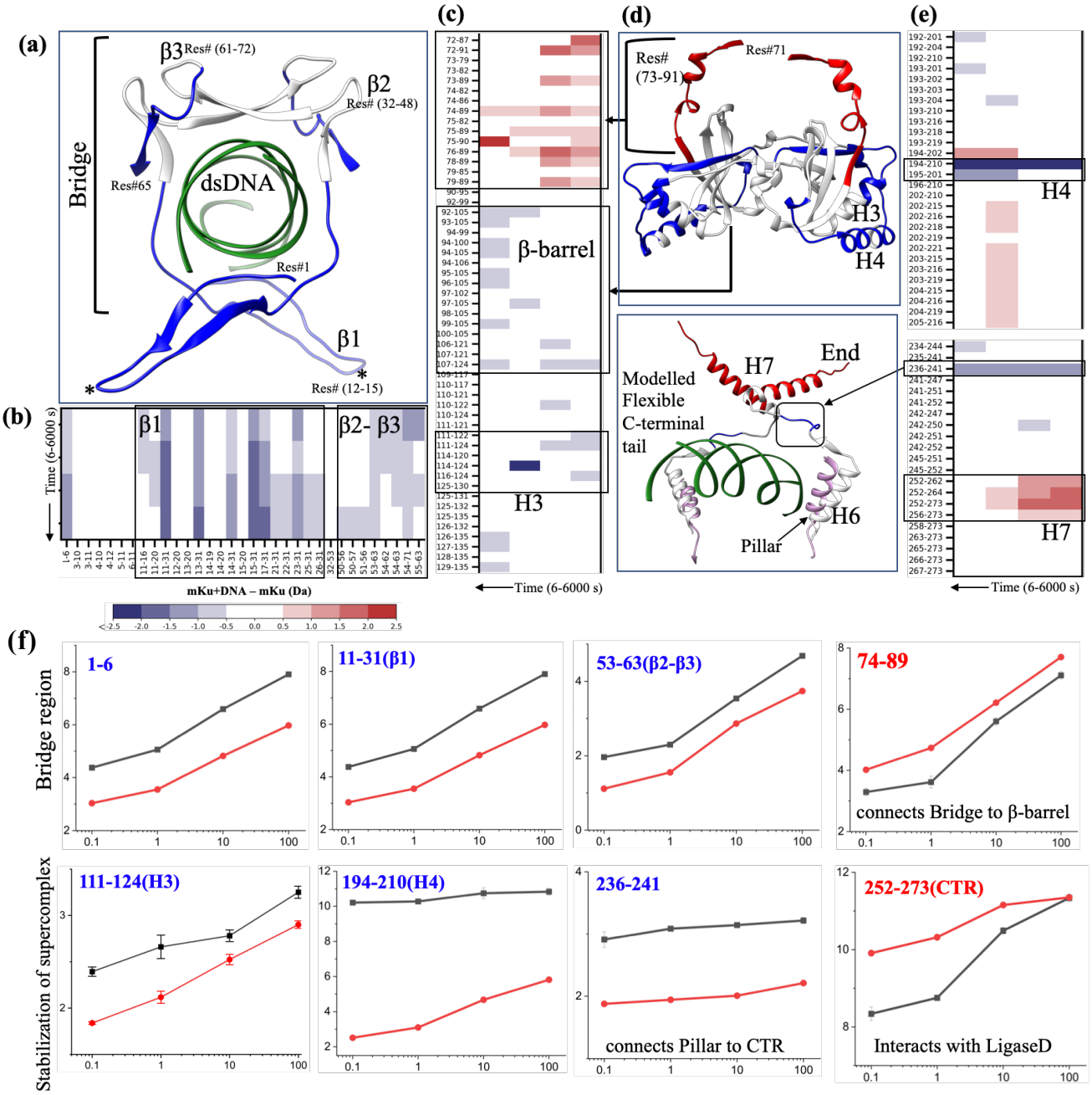

Figure 3 | HDX-MS analysis of protein-protein and DNA-protein interactions in the mKu and mKu-dsDNA complex: (a & d) Truncated model structures are colour-coded based on relative deuterium uptake: protected regions are shown in blue, while deprotected regions are depicted in red. The relative uptake represents the difference in D_2O incorporation (mKu-DNA minus mKu) for respective peptide stretches. (b, c & e) Chicklet plots illustrate global, time-dependent uptake profiles across 0.1–100 minutes. (f) Comparative local uptake plots highlight critical regions, with mKu-DNA in black and apo mKu in red. Plot labels are coloured blue or red, indicating protected or deprotected nature.

Figure 4 | DNA-mKu interactions

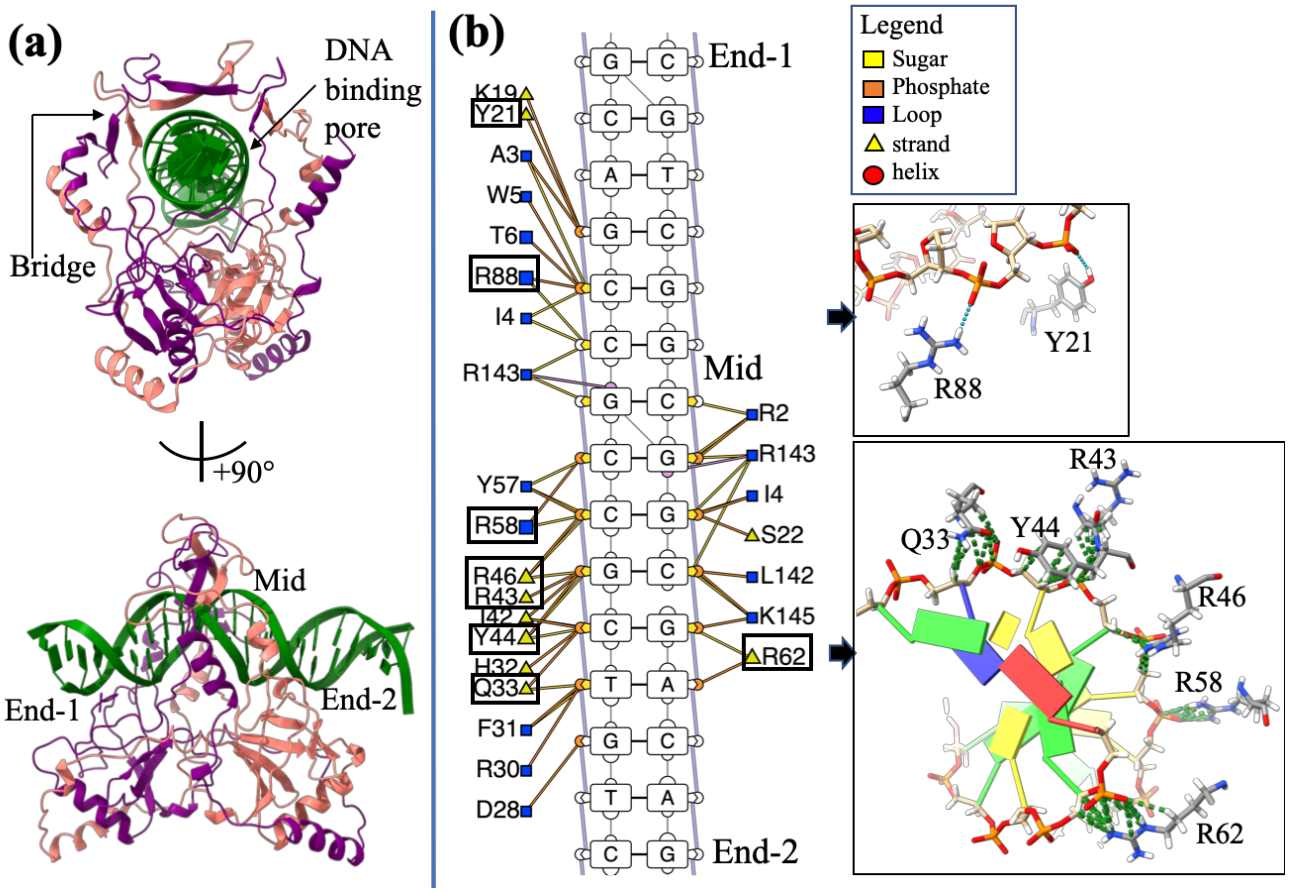

Figure 4 | **DNA-mKu interactions:** (a) Structural representation of the unit dimeric mKu-DNA complex, highlighting the DNA-binding pore of mKu and the regions of DNA contact. (b) 2D contact map illustrating DNA-protein interactions, with critical contacts detailed in the adjacent panel. Key contacts are indicated by green dotted lines.

Figure 5 | Higher order oligomerization of mKu directs DNA synapsis

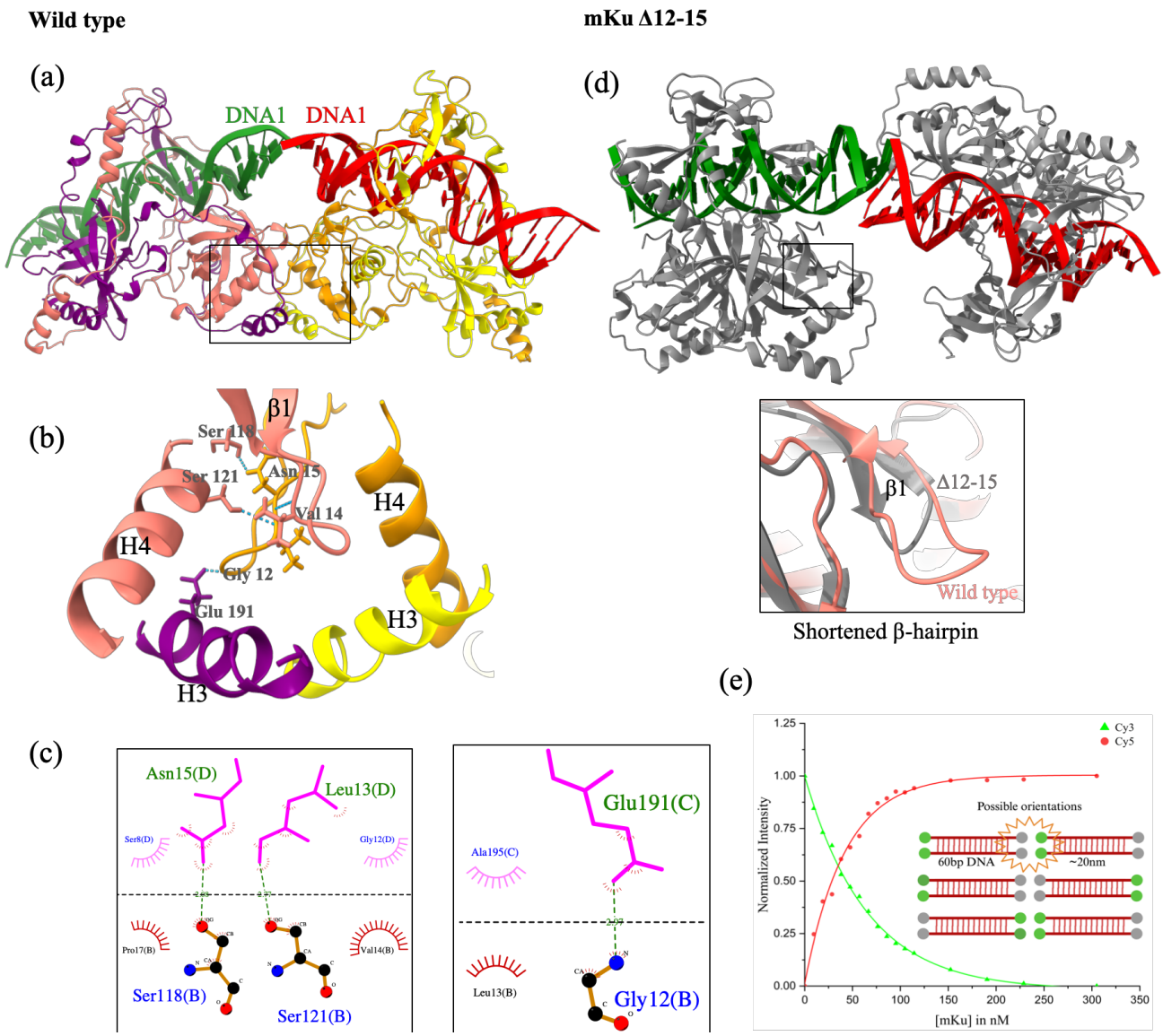

Figure 5 | Higher order oligomerization of mKu facilitates DNA synapsis: (a) Structure of the mycobacterial Ku-mediated DNA synaptic complex, with individual chains uniquely coloured to distinguish them. (b) Enlarged view of the β-hairpin1 interaction, highlighting residues 12–15 (GLVN), which are crucial for oligomerization. (c) 2D representation of atomic contacts between adjacent mKu homodimers, essential for forming the mKu-DNA supercomplex. Here, chains a-d represent individual mKu monomer (d) AlphaFold3-modeled structure of the mKuΔ12–15 mutant DNA complex, showing impaired DNA synapsis. The mKu dimers are depicted in grey, while the two DNA molecules are shown in red and green. A detailed view of the truncated β-hairpin1 in the mKuΔ12–15 mutant is provided below. (e) FRET assay results demonstrate that wild-type mKu forms stable DNA synapses, bringing broken DNA ends into proximity. The normalized fluorescence intensities of the donor (Cy3, green) and acceptor (Cy5, red) are plotted across a range of mKu concentrations (0–305 nM).

Figure 6 | Comparison between prokaryotic and eukaryotic DNA synapsis

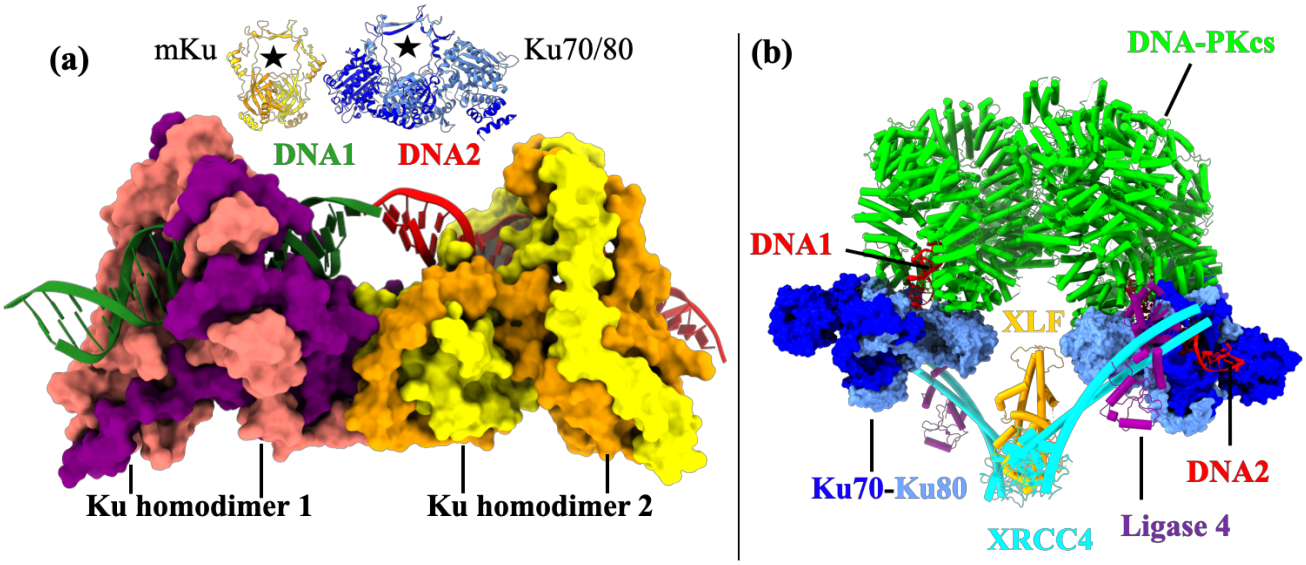

Figure 6 | Relative simplicity of prokaryotic DNA synapsis: (a) Structural representation of the mKu-mediated DNA synaptic complex of *Mycobacterium tuberculosis*, showing mKu homodimer 1 (purple and magenta) and homodimer 2 (orange and yellow) binding DNA 1 (green) and DNA 2 (red). At the top the dimeric structures of mycobacterial and human Ku are compared to highlight the size differences in their respective complexes, with stars indicating the DNA-binding pores of each Ku dimer. (b) Structural representation of the human long-range DNA synaptic complex, with individual components colour-coded as indicated (PDB: 7NFC, Chaplin *et al.,* 2021).

Figure 7 | Live cell imaging captures DNA damage response of mKu

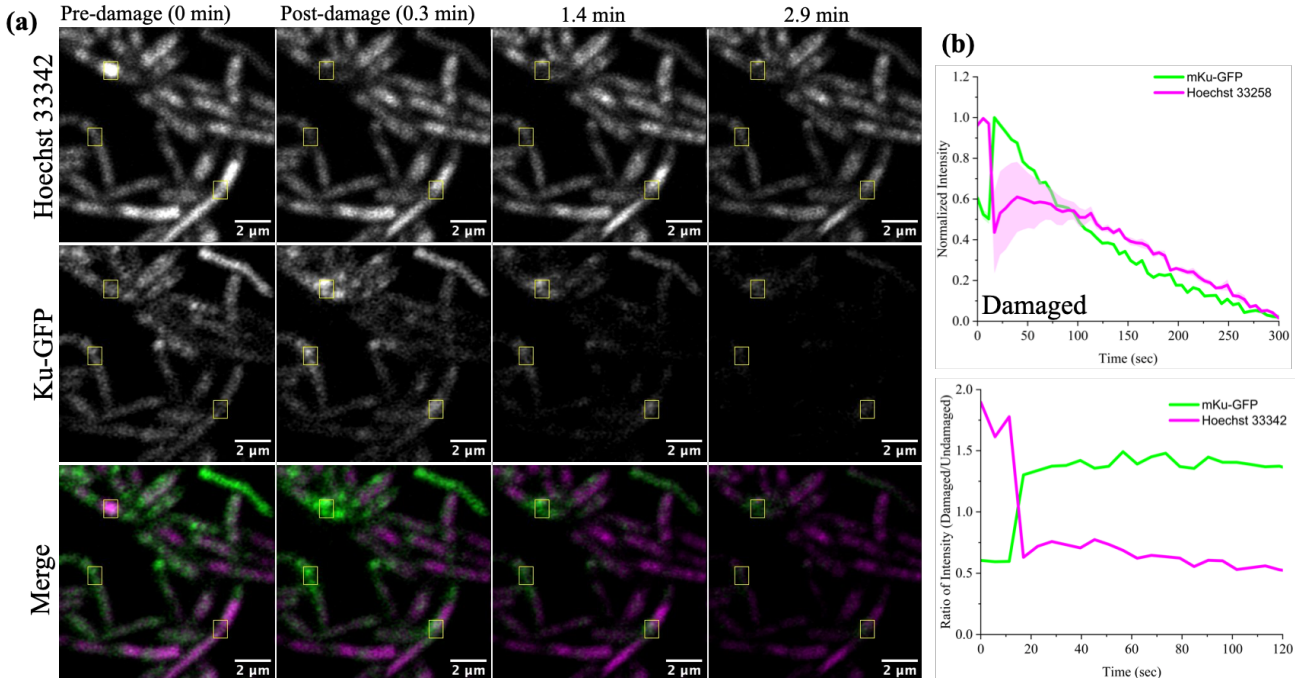

Figure 7 | Live cell imaging captures DNA damage response of mKu: (a) Dynamics of mKu-GFP shown pre- and post-laser-induced DNA damage. The laser damage is focused within a 0.8 µm x 1 µm region (yellow box); the control ROI has the same dimensions (not shown) but no laser damage. The dimensions of the boxes are scaled. DNA is stained with Hoechst 33342. (b) Intensity quantification over time, with magenta and green lines representing dynamics of DNA and mKu-GFP signals at damaged and undamaged ROI, respectively.